ARTICLE OPEN

Check for updates

Controlling the photon number coherence of solid-state quantum light sources for quantum cryptography

Yusuf Karli[1,9✉], Daniel A. Vajner[2,9], Florian Kappe[1,9], Paul C. A. Hagen[3], Lena M. Hansen[4,5], René Schwarz[1], Thomas K. Bracht[6,7], Christian Schimpf[8], Saimon F. Covre da Silva[8], Philip Walther[4,5], Armando Rastelli[8], Vollrath Martin Axt[3], Juan C. Loredo[4,5], Vikas Remesh[1], Tobias Heindel[2], Doris E. Reiter[6] and Gregor Weihs[1]

Quantum communication networks rely on quantum cryptographic protocols including quantum key distribution (QKD) based on single photons. A critical element regarding the security of QKD protocols is the photon number coherence (PNC), i.e., the phase relation between the vacuum and one-photon Fock state. To obtain single photons with the desired properties for QKD protocols, optimal excitation schemes for quantum emitters need to be selected. As emitters, we consider semiconductor quantum dots, that are known to generate on-demand single photons with high purity and indistinguishability. Exploiting two-photon excitation of a quantum dot combined with a stimulation pulse, we demonstrate the generation of high-quality single photons with a controllable degree of PNC. The main tuning knob is the pulse area giving full control from minimal to maximal PNC, while without the stimulating pulse the PNC is negligible in our setup for all pulse areas. Our approach provides a viable route toward secure communication in quantum networks.

npj Quantum Information (2024)10:17 ; https://doi.org/10.1038/s41534-024-00811-2

INTRODUCTION

Single photons are an essential resource for future high-security communication networks, with applications like measurement-based or distributed quantum computing and quantum cryptography[1–3]. Every quantum information protocol has its unique set of practical requirements[4]. While early quantum key distribution (QKD) protocols[5,6] primarily relied on high single-photon purity, more advanced schemes have further requirements such as high indistinguishability, for example, in quantum repeaters or measurement-device-independent (MDI)-QKD, which relies on remote two-photon interference[7,8]. The search for efficient single-photon sources has led to semiconductor quantum dots[9], thanks to their high single-photon purity[10], brightness[11], indistinguishability[12], scalability[13], and above all, versatility in emission wavelength selection.

Photon number coherence (PNC)[14,15] is another crucial quantity relevant to the security of single-photon quantum cryptography schemes. In the ideal case, a single photon can be represented by the one-photon Fock state, but due to imperfections or coupling to the environment, other Fock states can become occupied as well. The unwanted occupation of the two-photon Fock state is reflected by a reduced single-photon purity. In contrast, the occupation of the vacuum state is not accounted for in a correlation measurement. Instead, the PNC gives information on the influence of the vacuum state, as it is defined as the phase relation between vacuum and one-photon Fock state. This deviation from the one-photon Fock state can compromise security[16,17], but might also be a resource for advanced QKD protocols[18].

For most protocols[18], the PNC compromises the security[16,17] and therefore must vanish. Security is impaired by side-channel attacks enabled by the fixed relative phase between different photon number states[19,20]. While there are more general security proofs that allow a non-zero PNC, they lead to lower key rates, as some of the bits must be devoted to compensate for the additional information leakage towards an eavesdropper[21]. To achieve zero PNC in practice, actively phase-randomized single photons can be used, as typically implemented for faint laser pulses[22,23]. Otherwise, a suitable excitation scheme without PNC must be chosen, which might however deteriorate other single-photon properties[14,18].

Due to its versatility, the excitation scheme presented here covers the requirements of a broad range of quantum cryptographic protocols. An overview of various applications in the context of PNC and indistinguishability requirements is given in Fig. 1. For example, established protocols like BB84[5], decoy-BB84[24], 6-state-protocol[25], SARG04[26], LM05[27] and primitives like strong quantum coin flipping[28,29], unforgeable quantum tokens[30,31], quantum bit commitment[32] or quantum oblivious transfer[33] require the absence of PNC to ensure, for instance, security in QKD or fairness in coin-flipping protocols. On the other hand, there exist protocols that benefit from a finite amount of initial PNC like MDI-QKD when done with phase encoding[8] or twin-field QKD protocols[34] to know and set the initial phase[18]. Therefore, besides proper knowledge of the degree of PNC, one also requires a way to tune it, thereby enabling a wide range of quantum cryptographic applications.

In this work, we achieve tailored degrees of PNC from a quantum dot photon source, on-demand, assuring high purity and

[1]Institut für Experimentalphysik, Universität Innsbruck, 6020 Innsbruck, Austria. [2]Institute of Solid State Physics, Technische Universität Berlin, 10623 Berlin, Germany. [3]Theoretische Physik III, Universität Bayreuth, 95440 Bayreuth, Germany. [4]University of Vienna, Faculty of Physics, Vienna Center for Quantum Science and Technology (VCQ), Vienna, Austria. [5]Christian Doppler Laboratory for Photonic Quantum Computer, Faculty of Physics, University of Vienna, Vienna, Austria. [6]Condensed Matter Theory, Department of Physics, TU Dortmund, 44221 Dortmund, Germany. [7]Institut für Festkörpertheorie, Universität Münster, 48149 Münster, Germany. [8]Institute of Semiconductor and Solid State Physics, Johannes Kepler University Linz, 4040 Linz, Austria. [9]These authors contributed equally: Yusuf Karli, Daniel A. Vajner, Florian Kappe.
✉email: yusuf.karli@uibk.ac.at

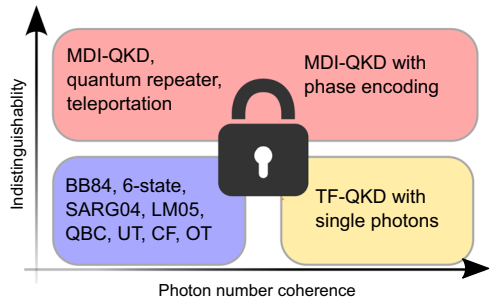

Fig. 1 Overview of various quantum information protocols. The protocols are sorted by their requirements on indistinguishability $\mathcal{I}$ and PNC, specifically focusing on discrete variable cryptographic protocols using polarization or time-bin encoding. Protocols that require low PNC and need no high $\mathcal{I}$ are BB84[5], decoy-BB84[24], 6-state-protocol[25], SARG04[26], LM05[27], QBC: quantum bit commitment[32], UT: unforgeable quantum tokens[30,31], CF: quantum coin flipping[28,29], OT: Oblivious Transfer[59]; low PNC and high $\mathcal{I}$ is required by MDI-QKD[8], quantum repeaters and entanglement swapping for QKD[7,60], quantum teleportation for QKD[61], DI-QKD with single photons[62]; high PNC and variable $\mathcal{I}$ are needed in TF: twin-field QKD with single photons[34]. Note that carrying out protocols from the low PNC column with phase encoding would require an initially defined phase, before randomizing it in a reversible way, which requires PNC in the beginning. To illustrate this we have also added MDI-QKD with phase encoding to the diagram.

indistinguishability. Our optical excitation protocol helps generate single-photon states in a well-defined polarization basis, and the photon counts are almost twice as large as achieved by the resonant excitation. We therefore set the stage for our quantum dot platform for its use in advanced cryptographic implementations.

RESULTS

Two-photon excitation of quantum dots

Being excellent photon sources, we choose to work with semiconductor quantum dots. The quantum dot can be modeled as a four-level system with the ground state $|g\rangle$, two linearly polarized exciton states $|x_{V/H}\rangle$ and a biexciton state $|xx\rangle$ as depicted in Fig. 2a. Among the different excitation protocols available[35], we choose the ones that are based on resonant two-photon excitation (TPE) of the quantum dot from the ground state $|g\rangle$ into the biexciton state $|xx\rangle$[36,37] with the experimental setup shown in Fig. 2d.

The TPE excitation leads to Rabi rotations between the ground and the biexciton state. The TPE pulse area π is defined such that the biexciton state occupation is maximum. A simulation of TPE Rabi rotations, i.e., the biexciton occupation as a function of pulse area, is shown in Fig. 2b. The oscillatory behavior of the Rabi rotations is clearly visible also in the measurement (Fig. 2c). The TPE excitation is a coherent excitation method, in contrast to the incoherent excitation methods like phonon-assisted state preparation[38]. Thus, the coherence between ground and exciton state builds up, whenever a superpositon state is reached, e.g., for a $\pi/2$ pulse. In contrast to the ideal case (dashed lines), in reality, the coupling to the environment, i.e., to phonons and radiative losses into the photonic environment, disturbs the Rabi rotations. The simulations for an environment at $T = 1.5$ K (solid lines) show that the maximal occupation is reduced, but more importantly for later, the oscillation of the coherence is less pronounced. In particular, it does not reach zero anymore at the π-pulse.

From the biexciton state, the system relaxes into either horizontally $|x_H\rangle$ or vertically $|x_V\rangle$ polarized exciton state, from which we collect only horizontally (H) polarized photons. We call this scheme *relaxation into the exciton* (reX). The reX scheme is advantageous over the direct, resonant excitation of the exciton, due to the suppressed re-excitation and therefore provides high-purity photon states[10]. Because the exciting laser energy is different from the emitted photon energy, a challenging cross-polarization filtering is avoided which is also achieved by several other recently proposed excitation schemes[39–45]. However, the indistinguishability of the single photons via the reX scheme suffers greatly from the spontaneous decay of the biexciton[46] and if a specific polarization is required, the photon output is reduced due to the two available decay channels.

An improved protocol to overcome these problems uses an additional stimulation laser pulse following the TPE pulse[47]. This *stimulated preparation of the exciton* (stiX) scheme can generate higher indistinguishability exciton photons due to the reduced time jitter[48–50]. Because the stimulation pulse determines the polarization of the emitted photon, the photon counts in that polarization state are also enhanced up to a factor of two (see also Fig. 2c). Although the presence of PNC under resonant excitation and reX has been investigated before[14,18], it remains to be seen if PNC exists in the stiX scheme. Additionally, assessing the controllability of PNC is essential for advancing optical preparation schemes of quantum dot states for quantum cryptography applications.

Definition of photon number coherence

Following the optical excitation, the quantum dot will emit a specific photon state, which can either be a pure state or a statistical mixture. In a pure photon state $|\Psi\rangle = \sum_{n=0}^{\infty} c_n|n\rangle$, written in the photon number Fock basis with eigenstates $|n\rangle$ and the complex coefficients c_n, we define PNC as the absolute value of the coherence between the Fock states. For QKD based on single photons, as considered in this paper, the PNC refers to the coherence between the Fock states $|0\rangle$ and $|1\rangle$. More generally and accounting also for statistical mixtures, we employ a density matrix description using

$$\rho = \begin{pmatrix} \rho_{0,0} & \rho_{0,1} \\ \rho_{1,0} & \rho_{1,1} \end{pmatrix} \quad \text{with} \quad \text{PNC} = |\rho_{0,1}|, \tag{1}$$

$\rho_{1,1}$ ($\rho_{0,0}$) being the occupation of the one (zero)-photon state and $\rho_{0,1}$ being the coherence. We recall that it holds that $|\rho_{0,1}|^2 \leq \rho_{1,1}\,\rho_{0,0}$ with equality in the case of a pure state. The inequality implies that for $\rho_{1,1} = 1$ or $\rho_{0,0} = 1$ the PNC vanishes, while for $\rho_{0,0} = \rho_{1,1} = 1/2$ it is maximal.

There are several factors that affect the PNC. One aspect is the imperfect control of the electronic system, from which the photon properties are inherited. The controllability of the electronic system of a quantum dot is known to be strongly influenced by the interaction with the lattice vibration, i.e., the phonons[35,51]. In addition, phonons can degrade the coherence properties of the photons[52] and therefore also the PNC. In addition to phonons, there are other loss channels that can further affect the photon properties, for example, losses of photons into other undetected modes.

It is likewise important to consider the measurement process. To detect PNC, a phase-evolving Mach-Zehnder Interferometer (MZI) is employed[14]. The outputs of the MZI are simultaneously recorded with two avalanche photodiodes (APDs). The count rates N_1, N_2 in the APD result in the visibility

$$v_i = \frac{N_i^{\max} - N_i^{\min}}{N_i^{\max} + N_i^{\min}}. \tag{2}$$

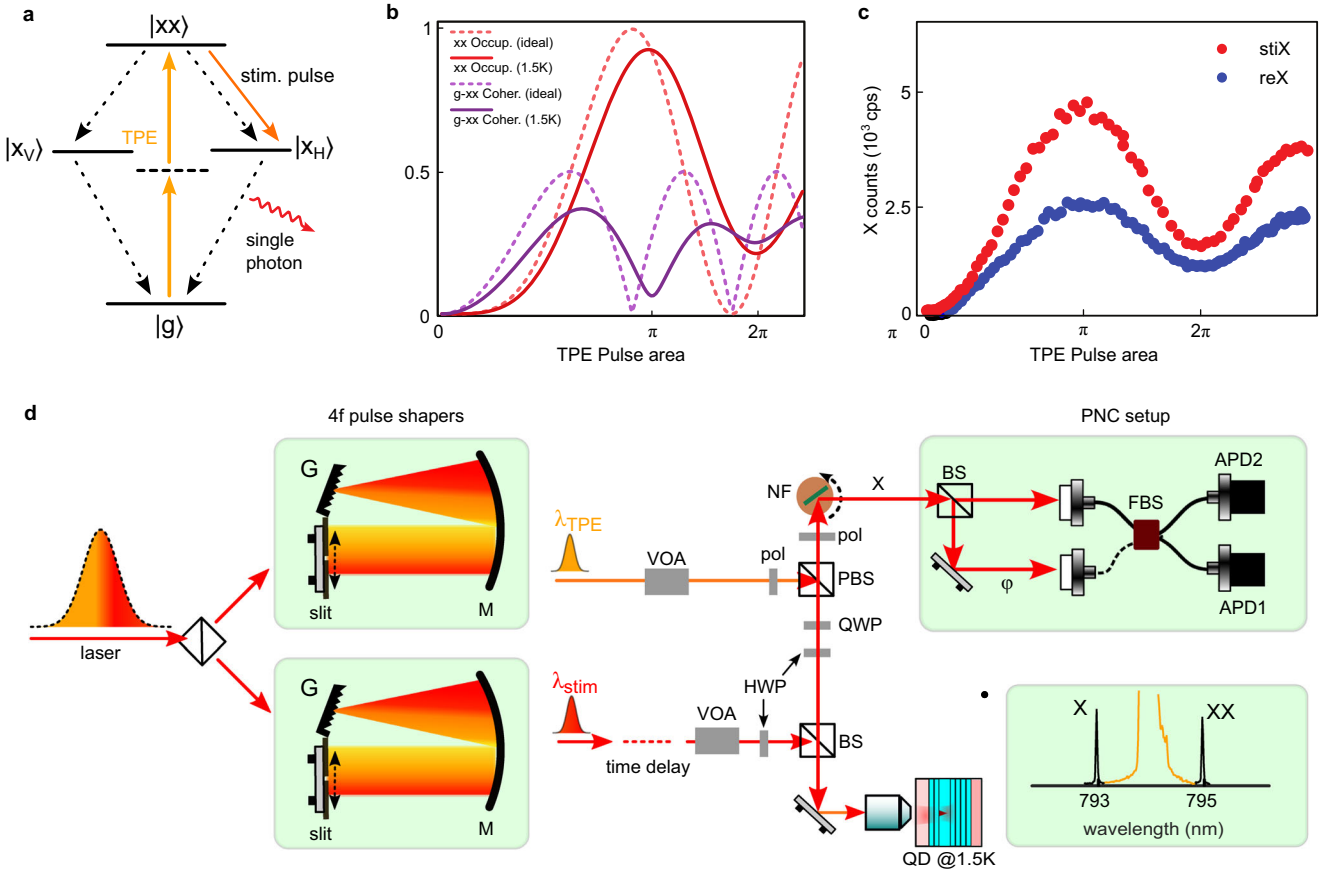

Fig. 2 Generating single photons with variable PNC. a Level scheme of a quantum dot consisting of the ground state $|g\rangle$, two linearly polarized exciton states $|x_{V/H}\rangle$ and biexciton state $|xx\rangle$. Straight lines indicate laser excitation, while dashed lines denote relaxation processes with rate γ. Both schemes start with a two-photon excitation (TPE) from $|g\rangle \rightarrow |xx\rangle$. In stiX, an additional H-polarized laser pulse stimulates the transition $|xx\rangle \rightarrow |x_H\rangle$. We only collect *H*-polarized photons. **b** Theoretically calculated biexciton ($|xx\rangle$) occupation showing Rabi rotations as a function of the TPE pulse area (red curve) and the corresponding coherence between $|g\rangle$ and $|xx\rangle$ (purple curve). **c** Exciton photon counts recorded under reX (blue dots) and stiX (red dots) manifest the enhancement of photon counts when the emission with a specific linear polarization is required. **d** Sketch of the experimental setup: a Ti:Sapphire laser source producing ≈ 2 ps-long laser pulses, with a spectral FWHM of 0.5 nm, is used to spectrally shape TPE and stim. pulses at appropriate wavelengths λ_{TPE} and λ_{stim} using two 4*f* pulse shapers. A fiber-optic delay line enables the time control of the stim. pulse with respect to the TPE pulse. An electronic variable optical attenuator (VOA) helps sweeping the laser power. The two pulses meet at a 10:90 beam splitter (BS) and propagate to the cryostat which holds the quantum dot at 1.5 K. Emitted single photons from the quantum dot are spectrally filtered by a notch filter (NF) and sent to an unbalanced Mach-Zehnder interferometer with a freely evolving phase on one arm (labeled as PNC setup). Two single-photon sensitive avalanche photodiodes (APD1 and APD2) detect the single-photon counts at the output arms of the interferometer. pol: linear polarizer, HWP: half-wave plate, QWP: quarter-wave plate, BS: beam splitter, PBS: polarizing beam splitter, FBS: fiber beam splitter.

In the case of an ideal measurement and perfectly indistinguishable photons, the visibility is connected to the PNC via

$$v = \frac{|\rho_{0,1}|^2}{\rho_{1,1}}. \tag{3}$$

In the MZI used in the experiment, the interference of subsequent single photons takes place. Phase scrambling between subsequent emission events leads to a further reduction of the visibility in addition to the aforementioned phonon and loss effects. It should be kept in mind that a vanishing visibility in the experiment can therefore result either from vanishing PNC, phase scrambling, or a combined effect of both.

Theoretical expectations

Initially, we perform theoretical simulations to estimate the PNC for both reX and stiX for a quantum dot modeled as a four-level system driven by a (classical) laser field and coupled to two discrete photon modes. The simulation considered the presence of three-photon states, however, only the vacuum and one-photon states were found to be noticeably populated. Note that the frequencies of the photon modes were set in resonance to the quantum dot transition from the ground to the exciton state and therefore direct two-photon emission is off-resonant. We further account for coupling with acoustic phonons within a numerically exact path-integral formalism[53]. In addition, we include the relaxation between the quantum dot states accounting for photons not being emitted into the relevant modes (see Methods section for details of the model and calculation). We assume an ideal detection, i.e., no phase scrambling and perfect indistinguishability and model the visibility via Eq. (3).

The time evolution of the biexciton and the $|x_H\rangle$ exciton occupation together with the PNC $|\rho_{0,1}|$ is shown in Fig. 3a, b. The laser sequence is shown in Fig. 3c. Both schemes start with an excitation from the ground into the biexciton state induced by a Gaussian-shaped laser pulse (orange curve in Fig. 3c) with a TPE pulse area of $\pi/2$. In the reX scheme, the biexciton state then relaxes into the exciton state via the emission of photons. However, these photons are at a different wavelength and therefore ignored. The exciton state is transiently occupied

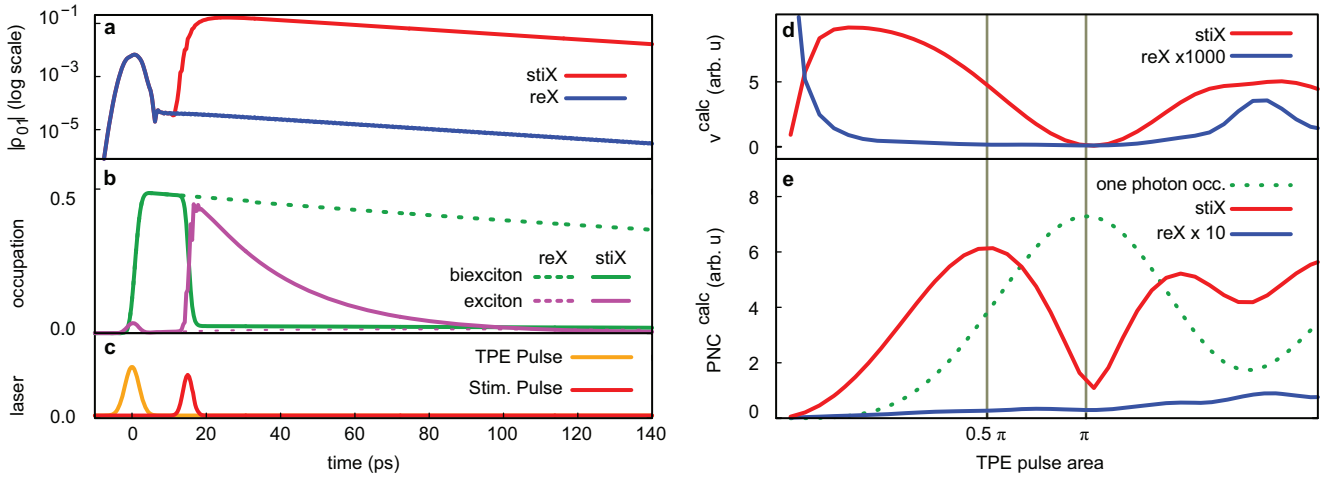

Fig. 3 Theoretical predictions. a, **b**, **c** Dynamics of the four-level system coupled to two-photon modes including phonons and losses calculated via a numerically exact path-integral formalism. The exciting laser pulses with the TPE pulse (orange) and stimulating pulse (red) are shown in **c**. The occupation of the biexciton and exciton state for stiX are displayed in **b** with the dashed line indicating the behavior for reX. The PNC for stiX (red) and reX (blue) is displayed in **a**. Note the logarithmic scale. During the stimulating pulse, the exciton becomes occupied resulting in a rise of the PNC. **d**, **e** Time-integrated coherence $\mathrm{PNC}^{\mathrm{calc.}}$ (**e**) and visiblity v^{calc} (**d**) as a function of TPE pulse area for both reX (blue, magnified) and stiX (red). The TPE pulse areas of π and $\pi/2$ are marked by vertical lines. The time-integrated occupation of the one-photon Fock state $\mathrm{occ.}^{\mathrm{calc}}$ is shown as a green dashed line. Due to the relaxation process, the PNC is almost lost in the reX case. In stiX, we find that the PNC is controlled via the TPE pulse area.

because it rapidly generates the desired photon relaxing further into the ground state. The corresponding PNC (blue curve in Fig. 3a) is almost vanishing, too, because of the incoherent biexciton-exciton relaxation destroying the electronic coherence. The remaining PNC can be traced back to deviations from the ideal case caused by phonon interaction, radiative losses, as well as relaxation into other (undesired) states in the quantum dot.

In contrast, in the stiX scheme, the stimulating pulse (red curve in Fig. 3c) brings the biexciton coherently into $|x_H\rangle$ by the application of a π-pulse resonant to the $|xx\rangle \rightarrow |x_H\rangle$ transition as evidenced in Fig. 3b. The small oscillations on top of the population-exchange result from the off-resonant driving of the complementary transition $|x_H\rangle \rightarrow |g\rangle$. Because the transition to the exciton state $|x_H\rangle$ is coherent, the electronic coherence, which translates to the PNC, is preserved. Accordingly, in Fig. 3a (red curve), we see that as soon as the stimulating pulse sets in, the PNC becomes very high. In other words, a timed stimulation preparation of the exciton state recovers the PNC that is lost in the reX scheme.

By controlling the electronic coherence through the pulse areas of the exciting pulses, we can thus manipulate the PNC. To ensure the best comparability, we fix the stimulating pulse to a π pulse and vary the pulse area of the TPE pulse. We remind that TPE is a coherent excitation and that the corresponding coherence oscillates as a function of pulse area (cf. Fig. 2b). The time-integrated occupation of the one-photon state $\mathrm{occ}^{\mathrm{calc}}$ follows the Rabi rotations of the biexciton (cf. Fig. 2b). We have checked that under the present conditions, the higher Fock states always have negligible occupations.

To estimate the PNC as a function of pulse area, we consider the time-integrated variable $\mathrm{PNC}^{\mathrm{calc}} = |\rho_{0,1}|$ in Fig. 3e. The $\mathrm{PNC}^{\mathrm{calc}}$ should follow the coherence oscillations of the electronic system, i.e., the coherence between ground and biexciton state. Thus, the highest PNC is expected for pulse areas $(2n+1)\pi/2$, where also the electronic coherence is maximal. However, due to the incoherent relaxation process from the biexciton into the exciton, in reX the $\mathrm{PNC}^{\mathrm{calc}}$ is close to zero for all pulse areas as expected. This is confirmed by the numerical results in Fig. 3e. Only for large pulse areas, detrimental processes due to phonons or losses lead to some residual $\mathrm{PNC}^{\mathrm{calc}}$.

The behavior changes totally for stiX, where the coherence is preserved due to the stimulating pulse. Hence we find an oscillating behavior of $\mathrm{PNC}^{\mathrm{calc}}$ as a function of the TPE pulse area. The maxima of the $\mathrm{PNC}^{\mathrm{calc}}$ coincide with the maxima of the electronic coherence as a function of the TPE pulse area, while the minima of the electronic coherence should lead to vanishing $\mathrm{PNC}^{\mathrm{calc}}$. In Fig. 3e maxima of $\mathrm{PNC}^{\mathrm{calc}}$ occur for TPE pulse areas $(2n+1)\pi/2$ and minima for pulse areas $n\pi$. Ideally, PNC should be zero for pulse areas $n\pi$. In the full simulation including finite pulse lengths and losses, the TPE pulse does not fully invert the system and the electronic coherence is reduced (cf. Fig. 2b). Additionally, the PNC itself is affected by environmental losses. This leads to a residual PNC even for a TPE π-pulse.

To compare with the experiment, we also compute the visibility v^{calc} in Fig. 3d. The visibility behaves differently compared to $\mathrm{PNC}^{\mathrm{calc}}$. While a clear minimum at π is recovered, the PNC is not maximal at $\pi/2$. Instead, due to its definition, v^{calc} increases for the even smaller TPE pulse areas. Still it remains true that, compared to reX, the visibility for stiX shows a strong dependence on the TPE pulse area.

Experimental data

We perform the reX and stiX experiments to test the theoretical prediction on a single quantum dot in our setup displayed in Fig. 2d. We note that in stiX we fix the time delay between the TPE pulse and stimulating pulse to 7 ps, where the photon count is maximal. A detailed description of the experiment is provided in the Methods Section.

We start by quantifying the photon properties for reX and stiX, at various powers (see Supplementary Table 1) measuring the single-photon purity in a Hanbury Brown and Twiss (HBT) setup and the indistinguishability via Hong-Ou-Mandel (HOM) measurements. At π power of both reX and stiX we validate that the generated photons have high purity with $g^{(2)}_{\mathrm{reX}}(0) = 0.0004(1)$ and $g^{(2)}_{\mathrm{stiX}}(0) = 0.0009(1)$. For the indistinguishability, the HOM visibility reaches only 58(3)% under reX, while for stiX it increases to 95(6)%, in line with previous observations[48–50]. These results already underline that stiX is advantageous over reX.

We then sweep the TPE pulse area under reX and stiX yielding Rabi rotations for the exciton (X) photon counts (blue and red

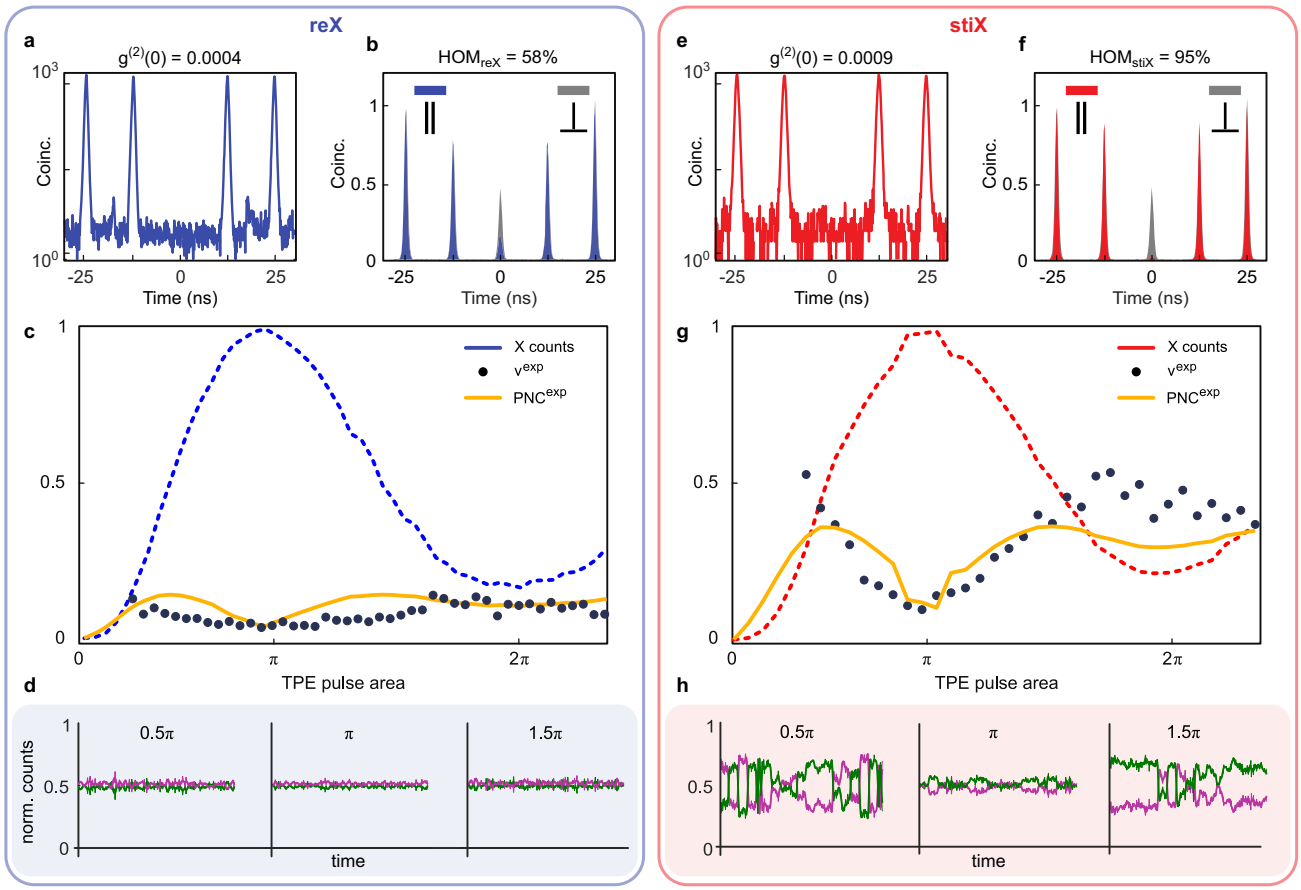

Fig. 4 Controlled generation of PNC on a single quantum dot for reX and stiX. a, **e** Measured purity of the generated single photons. **a** $g^{(2)}_{reX}(0)$ (blue), the TPE pulse power is kept at π-power, and the stim pulse is absent. **e** $g^{(2)}_{stiX}(0)$(red), TPE and stim pulses are kept at π-power. **b**, **f** HOM_{reX}, blue and gray shaded curves represent HOM coincidences recorded for parallel and orthogonal polarizations respectively, **b** for π TPE pulse area. HOM_{stiX}, red and gray shaded curves represent HOM coincidences recorded for parallel and orthogonal polarizations respectively, **f** TPE and stim pulses are kept at π-power. **c**, **g** Extracted visibilities v^{exp} (dark-blue dots) and the reconstructed PNC^{exp} (yellow) at different TPE pulse areas alongside the measured X counts (blue curve for X_{reX} and red curve for X_{stiX}). The X counts are normalized to their respective values at π-power. **d**, **h** Exemplary time traces were recorded at the two detector outputs of the PNC setup at TPE pulse areas of 0.5π, π and 1.5π.

curves in Fig. 4c, g), and investigate the PNC. For each TPE pulse power, we analyze the spectrally filtered X photons using a phase-evolving MZI[14]. Its outputs are simultaneously recorded with two avalanche photodiodes (APDs) for 20 s each. In Fig. 4d, h, we display exemplary time traces (denoted by green and magenta curves, representing the two detector outputs of the MZI, see also Fig. 2d) at TPE pulse areas 0.5π, 1π, 1.5π. From the time traces, we compute the visibility according to Eq. (2) from the normalized detector counts taking the average of the two detectors as $v^{exp} = (v_1 + v_2)/2$.

The visibility v^{exp} as a function of pulse area is displayed alongside the respective Rabi rotations in Fig. 4c, g as black dots. Under reX, the visibility v^{exp} is vanishing for all TPE pulse areas and no clear dependence is found. This is in agreement with the exemplary time traces (displayed in Fig. 4d), where indeed no oscillations are seen for different pulse areas.

In contrast, for stiX, the PNC shows a more interesting behavior: in the representative time traces of the MZI outputs (displayed in Fig. 4h), we observe clear oscillations for TPE powers 0.5π, and 1.5π and almost no oscillations at π. Accordingly, the visibilities vary from ≈ 0.6 at TPE power 0.5π to being minimal at π and then rise again until 1.5π.

From the visibilities, using the formalism from ref. [14], we extract the $PNC^{exp.}$ shown as the yellow line in Fig. 4c, g. In the formalism $PNC^{exp.}$ is reconstructed via the so-called λ-parameter, which is gained from the visibilities. Hence, a larger parameter range can be gained for $PNC^{exp.}$ then for the visibilities (cf. SI).

The data clearly confirms the trend expected from the theory: We find minima of PNC when exciting with TPE pulses of pulse area $n\pi$ and maxima at $(2n + 1)\pi/2$. This behavior is evident in stiX, while in reX only a small modulation is found.

Hence, we conclude that the PNC is negligible in reX, while in stiX we have tuneable PNC controlled via the TPE pulse area.

DISCUSSION

We now set our results in the context of finding the optimal photon source for high-security quantum networks. As indicated before, purity, indistinguishability, and PNC are the key parameters that must be known when choosing an excitation scheme. We have shown that reX generates high-purity photons, while indistinguishability and PNC are low, and also, if filtering only a single polarization, the photon output is reduced. Looking back at Fig. 1, we find that reX produces photons in the bottom left corner with low PNC and low indistinguishability, which limits the range of applicable protocols.

With the stiX method, photons with high purity and high indistinguishability are generated. More importantly, the PNC can

be controlled via the TPE pulse area. If the TPE power is set to $(2n+1)\pi/2$, one obtains high PNC, enabling protocols in the top right corner of the diagram in Fig. 1. By changing the pulse area to $n\pi$, the PNC is minimal while indistinguishability is maintained high, enabling protocols in the top left corner of the diagram in Fig. 1. For all TPE powers, stiX is the superior method for generating single photons for protocols that require high indistinguishability.

So far, we have discussed the TPE pulse area as the main control parameter for the time-integrated PNC. But stiX offers a much richer parameter space for tuning the PNC. As the stiX scheme is composed of two pulses, there is a wide playground of control options. We display additional control parameters in Supplementary Fig. 4. By varying the time delay between the TPE and the stimulating pulse, first a relaxation and then a stimulation occurs. This leads to a varying PNC as a function of time delay with loss of PNC for increasing time delays. More remarkably, the time delay control offers a different type of control compared to the pulse area control, because changing the time delay also affects the indistinguishability as indicated in Supplementary Fig. 5a.

In addition, we explored the polarization of the stimulating laser pulse showing high PNC and high indistinguishability in the chosen polarization basis (see Supplementary Fig. 5).

In summary, we showed the generation of single photons with variable degrees of PNC as well as high purity, high indistinguishability, and high brightness via a two-photon excitation combined with a stimulating pulse. This is a significant step forward towards the realization of secure quantum networks based on single photons.

METHODS

Theoretical model

For the theoretical modeling, we set up the Hamiltonian consisting of the quantum dot system $\hat{H}^{\mathrm{QD}}$, the out-coupling to two-photon modes $\hat{H}^{\mathrm{photon}}$, the excitation of the TPE $\hat{H}^{\mathrm{TPE}}$ and the stimulating laser pulse $\hat{H}^{\mathrm{stim}}$, as well as the coupling to phonons

$$\hat{H} = \hat{H}^{\mathrm{QD}} + \hat{H}^{\mathrm{photon}} + \hat{H}^{\mathrm{TPE}} + \hat{H}^{\mathrm{stim}} + \hat{H}^{\mathrm{phonon}}. \tag{4}$$

In addition, we consider radiative decay and losses by a Lindblad operator $\mathcal{L}$. In the following, we describe the individual terms in detail.

The quantum dot is modeled using four states (see also Fig. 2b) denoted by $|g\rangle$ as the ground state, $|x_H\rangle$ and $|x_V\rangle$ as the two excitons and $|xx\rangle$ as the biexciton. The ground-state energy is set to zero, while both excitons have the same energy $\hbar\omega_x$, i.e., no fine-structure splitting is assumed. The biexciton has a binding energy E_B such that its energy is given by $\hbar\omega_{xx} = 2\hbar\omega_x - E_B$.

$$\hat{H}^{\mathrm{QD}} = \hbar\omega_x(|x_H\rangle\langle x_H| + |x_V\rangle\langle x_V|) + \hbar\omega_{xx}|xx\rangle\langle xx| \tag{5}$$

The quantum dot is coupled to two-photon modes with polarizations V and H for the out-coupling of the photons, similar to positioning the quantum dot in a photonic cavity. We model the photon modes by the Fock states $|n_H\rangle$ and $|n_V\rangle$ with the frequency ω_c via the annihilation (creation) operators $\hat{a}_{H/V}(\hat{a}^\dagger_{H/V})$. The photonic modes are coupled to the quantum dot transitions with the same strength via the coupling constant $\hbar g = 0.05\mathrm{meV}$, yielding

$$\begin{aligned}\hat{H}^{\mathrm{photon}} &= \hbar\omega_c\left(\hat{a}^\dagger_H\hat{a}_H + \hat{a}^\dagger_V\hat{a}_V\right)\\ &\quad + \hbar g\,\hat{a}_H(|x_H\rangle\langle g| + |xx\rangle\langle x_H|) + h.c.\\ &\quad + \hbar g\,\hat{a}_V(|x_V\rangle\langle g| + |xx\rangle\langle x_V|) + h.c.\\ &= \hat{H}^{\mathrm{photon}}_0 + \hat{H}^{\mathrm{photon}}_{\mathrm{coupl.}}.\end{aligned} \tag{6}$$

We use the Hamiltonian in a rotating frame with $\omega = \omega_l = \omega_x - E_B/(2\hbar)$, which corresponds to the frequency of the TPE laser pulse. With this, the QD-photon Hamiltonian has the form

$$\begin{aligned}\hat{H}^{\mathrm{QD-photon}} &= \hbar\Delta\omega_{x-l}(|x_H\rangle\langle x_H| + |x_V\rangle\langle x_V|)\\ &\quad + (\hbar 2\Delta\omega_{x-l} - E_B)|xx\rangle\langle xx|\\ &\quad + \hbar\Delta\omega_{c-l}\left(\hat{a}^\dagger_H\hat{a}_H + \hat{a}^\dagger_V\hat{a}_V\right)\\ &\quad + \hat{H}^{\mathrm{photon}}_{\mathrm{coupl.}}.\end{aligned} \tag{7}$$

The index convention of frequency differences is chosen such that the second index is subtracted from the first, e.g., $\Delta\omega_{x-l} = \omega_x - \omega_l$. We choose the photon mode to be resonant with the quantum dot transition from the ground to the excited state, i.e., $\hbar\Delta\omega_{c-x} = 0$ meV.

The TPE is modeled by an external classical laser field with diagonal polarization in dipole and rotating wave approximation. We consider a resonant TPE process and accordingly set the detuning $\Delta\omega_{x-l} = E_B/(2\hbar)$. With this, the Hamiltonian reads

$$\begin{aligned}\hat{H}^{\mathrm{TPE}}(t) &= -\tfrac{\hbar}{2}f^{\mathrm{TPE}}(t)(|g\rangle\langle x_H| + |g\rangle\langle x_V|\\ &\quad + |x_H\rangle\langle xx| + |x_V\rangle\langle xx| + h.c.).\end{aligned} \tag{8}$$

Here, $f^{\mathrm{TPE}}(t)$ denotes the instantaneous Rabi frequency as given by the product of dipole moment and electric field. We use Gaussian pulses

$$f^{\mathrm{TPE}}(t) = \frac{\Theta_{\mathrm{TPE}}}{\sqrt{2\pi}\,\sigma_{\mathrm{TPE}}}\mathrm{e}^{-\frac{t^2}{2\sigma^2_{\mathrm{TPE}}}}, \tag{9}$$

with the pulse area Θ_{TPE} and the pulse width σ_{TPE}. We assign the TPE pulse area π in the plot (cf. Fig. 3 to the one which results in the first maximum of the biexciton occupation and the TPE pulse area of $\pi/2$ to the first maximum of the electronic coherence. In the calculations, these values were determined numerically.

We describe the stimulating laser with the same approximations, but assume it to be horizontally polarized. Its frequency is set to match the $|xx\rangle \rightarrow |x_H\rangle$ transition, such that

$$\begin{aligned}\hat{H}^{\mathrm{stim}}(t) = -\tfrac{\hbar}{2}f^{\mathrm{stim}}(t)\Big[&\mathrm{e}^{i\Delta\omega^{\mathrm{stim}}_l t}(|g\rangle\langle x_H|\\ &+ |x_H\rangle\langle xx|)\Big] + h.c..\end{aligned} \tag{10}$$

Here, $\Delta\omega^{\mathrm{stim}}_l = \omega^{\mathrm{stim}}_l - \omega_l = -E_B/(2\hbar)$. The stimulating laser's envelope function f^{stim} is delayed by a time Δt compared to the TPE laser. We also assume a Gaussian envelope for the stimulating pulse

$$f^{\mathrm{stim}}(t) = \frac{\Theta_{\mathrm{stim}}}{\sqrt{2\pi}\,\sigma_{\mathrm{stim}}}\mathrm{e}^{-\frac{(t-\Delta t)^2}{2\sigma^2_{\mathrm{stim}}}}. \tag{11}$$

with the pulse area Θ_{stim} and the pulse length σ_{stim}. Here, a "π-pulse" refers to a full inversion of the resonantly driven transition for ideal conditions (without losses/phonons).

In addition we consider the coupling to longitudinal-acoustic (LA) phonons via the deformation potential coupling. Here, $\hat{b}_{\mathbf{k}}$ ($\hat{b}^\dagger_{\mathbf{k}}$) annihilates (creates) a phonon of mode $\mathbf{k}$ with energy $\omega_{\mathbf{k}}$. We consider the typical pure-dephasing type coupling in the standard Hamiltonian[54,55]

$$\begin{aligned}\hat{H}^{\mathrm{phonon}} &= \hbar\sum_{\mathbf{k}}\omega_{\mathbf{k}}\hat{b}^\dagger_{\mathbf{k}}\hat{b}_{\mathbf{k}}\\ &\quad + \hbar\sum_{\mathbf{k},S}\left(\gamma^S_{\mathbf{k}}\hat{b}^\dagger_{\mathbf{k}} + \gamma^{S^*}_{\mathbf{k}}\hat{b}_{\mathbf{k}}\right)|S\rangle\langle S|,\end{aligned} \tag{12}$$

coupling each mode $\mathbf{k}$ to the quantum dot state $|S\rangle$, where $S \in \{x_H, x_V, xx\}$. The coupling constant $\gamma^S_{\mathbf{k}}$ and the material parameters are taken to be the same as in ref. [53].

Both, the cavity and quantum dot, are subject to losses into the free photonic field outside of the cavity. These losses are described by Lindblad-superoperators, affecting the density

operator $\hat{\rho}$

$$\mathcal{L}_{\hat{O},\delta}[\hat{\rho}] = \delta\left(\hat{O}\hat{\rho}\,\hat{O}^{\dagger} - \frac{1}{2}\left[\hat{\rho}, \hat{O}^{\dagger}\hat{O}\right]_{+}\right), \tag{13}$$

where $\hat{O}$ is an operator, δ a rate and $[.,.]_+$ the anti-commutator. We assume that the decay processes of the quantum dot take place with rate γ and losses of the photonic modes go with the rate κ, such that Lindblad-superoperators are

$$\begin{aligned}\mathcal{L}[\hat{\rho}] \;:=\; & \mathcal{L}_{\hat{a}_H,\kappa}[\hat{\rho}] + \mathcal{L}_{\hat{a}_V,\kappa}[\hat{\rho}] \\ & + \mathcal{L}_{|g\rangle\langle x_H|,\gamma}[\hat{\rho}] + \mathcal{L}_{|g\rangle\langle x_V|,\gamma}[\hat{\rho}] \\ & + \mathcal{L}_{|x_H\rangle\langle xx|,\gamma}[\hat{\rho}] + \mathcal{L}_{|x_V\rangle\langle xx|,\gamma}[\hat{\rho}]\,.\end{aligned} \tag{14}$$

The rates are chosen such that we are in the weak coupling regime.

With the Hamiltonian and the Lindbladian terms we calculate the dynamics of the system states via the Liouville-von Neumann equation

$$\frac{\mathrm{d}}{\mathrm{d}t}\hat{\rho} = -\frac{i}{\hbar}\left[\hat{H}(t), \hat{\rho}\right] + \mathcal{L}[\hat{\rho}]. \tag{15}$$

As the initial state, we assume that the quantum dot is in its ground state and no photonic excitation exists. For the numerical integration, we use a numerically complete path-integral method, which is described in refs. [53,56] and the parameters from Table 1, to solve Eq. (15).

We obtain results for the full density matrix, from which we can obtain the reduced density matrices for the quantum dots $\rho^{\mathrm{QD}}_{S,S'}$ with $S \in \{g, x_H, x_V, xx\}$ and for the photons $\rho^{\mathrm{photon}}_{n_i,n_i'}$ with $i \in \{H, V\}$, by tracing out the other degrees of freedom. We are interested in the coherence $\rho_{0,1} = \rho^{\mathrm{photon}}_{0_H,1_H}$. The absolute value of $\rho_{0,1} = \rho^{\mathrm{photon}}_{0_H,1_H}$ is referred to as PNC.

As a measure for the overall PNC at a given pulse area, we introduce the time-integrated absolute value of the instantaneous PNC

$$\mathrm{PNC}^{\mathrm{calc}} \propto \tilde{\rho}_{0,1} = \int |\rho^{\mathrm{photon}}_{0_H,1_H}| dt\,. \tag{16}$$

$\mathrm{PNC}^{\mathrm{calc}}$ is the calculated quantity that corresponds with the experimental quantity $\mathrm{PNC}^{\mathrm{exp}}$ below in Eq. (20).

Analogously, we define the time-integrated occupation of the one-photon number states as

$$\mathrm{occ}^{\mathrm{calc}} \propto \tilde{\rho}_{1,1} = \int \rho^{\mathrm{photon}}_{1_H,1_H} dt\,. \tag{17}$$

We assume that the photonic space can be reduced to a two-level system consisting of $|0_H\rangle$ and $|1_H\rangle$. This is reasonable because the higher-order Fock states are not occupied. We then follow ref. [14]

Table 1. Parameters used in the simulation.

QD-cavity detuning	$\hbar\Delta\omega_{c-x}$	0 meV
QD-laser detuning	$\hbar\Delta\omega_{x-l}$	2 meV
detuning stim. pulse	$\hbar\Delta\omega_l^{\mathrm{stim}}$	2 meV
duration stim. pulse	$\mathrm{FWHM}_{\mathrm{stim}}$	3 ps
duration TPE pulse	$\mathrm{FWHM}_{\mathrm{TPE}}$	4.5 ps
delay between pulses	Δt	15 ps
QD-cavity coupling	$\hbar g$	0.05 meV
Binding energy	E_B	4 meV
cavity loss rate	κ	0.577 ps^{-1}
QD loss rate	γ	0.001 ps^{-1}
QD size	a	3 nm
temperature	T	1.5 K

Material parameters are taken as in ref. [53].

to calculate the visibility v as measured in an MZI for a mixed state as

$$v^{\mathrm{calc}} = \frac{\tilde{\rho}^2_{0,1}}{\tilde{\rho}_{1,1}}\,. \tag{18}$$

We stress that this is an estimate of the visibility, which does not account for the imperfection of the beam splitter, higher photon states, phase scrambling, or reduced indistinguishability. Nonetheless, we expect the qualitative behavior to agree with the experiment.

Experimental setup

Our setup (Fig. 2d) consists of a Ti:Sapphire laser source (Tsunami 3950, SpectraPhysics) producing 2.7 ps pulses (measured as intensity autocorrelation FWHM), that is tuned to 793 nm, enabling spectral shaping of both the TPE and stimulating (stim). pulses via two independent 4*f* pulse shapers. The intensities of the TPE and stim pulses are individually controlled via electronic variable optical attenuators (VOA, V800PA, Thorlabs) and the arrival time of the stimulating pulse is precisely controlled via a fiber-optic delay line (ODL-300, OZ Optics). The two beams are combined at a 10:90 beam splitter near the optical window of a closed-cycle cryostat (base temperature 1.5 K, ICEOxford) where the quantum dot sample is mounted on a three-axis piezoelectric stage (ANPx101/ANPz102, attocube systems AG). The two beams are focused on a single quantum dot with a cold objective (numerical aperture 0.81, attocube systems AG).

Our sample consists of GaAs/AlGaAs quantum dots with exciton emission centered around 790 nm grown by the Al-droplet etching method[57,58]. The dots are embedded in the center of a lambda-cavity placed between a bottom (top) distributed Bragg reflector consisting of 9 (2) pairs of $\lambda/4$ thick $Al_{0.95}Ga_{0.05}As$/$Al_{0.2}Ga_{0.8}As$ layers.

The quantum dot emission is collected via the same path as the excitation, where the exciton (X) photons are spectrally separated from the scattered laser light and phonon side bands using a home-built monochromator equipped with two narrow-band notch filters (BNF-805-OD3, FWHM 0.3 nm, Optigrate). To improve the suppression of the reflected TPE pulse we employ a cross-polarized configuration in which two orthogonal linear polarizers on excitation and collection paths block any residual laser scattering. In fact, this would not be necessary for a sufficiently narrow laser spectrum, as the TPE energy is detuned from the exciton energy.

To measure the spectra, collected photons are routed to a single-photon sensitive spectrometer (Acton SP-2750, Roper Scientific) equipped with a liquid Nitrogen-cooled charge-coupled device camera (Spec10 CCD, Princeton Instruments). For lifetime measurements, we use an avalanche photodiode (SPAD, Micro Photon Device) together with time-tagging electronics.

To measure the indistinguishability, the filtered X photons are sent through a Mach-Zehnder Interferometer (MZI) with a path-length difference of 12.5 ns, to interfere with successively emitted photons from the quantum dot in a 50:50 fiber beam splitter (TW805R5A2, Thorlabs) for HOM measurement. The two output ports of the fiber beam splitter are monitored by avalanche photodiodes (SPCM-NIR, Excelitas). The arrival times of the photons are recorded using a time tagger (Time Tagger Ultra, Swabian Instruments), and coincidence counting is employed to determine the correlation between the photons. In the HOM measurement, the polarization in both MZI arms is controlled individually, enabling a comparison between the co-polarized scenario with maximum indistinguishability and the cross-polarized situation with distinguishable photons to obtain the HOM visibility.

For PNC measurements, a phase shifter is placed into one of the arms of the unbalanced MZI. The phase shifter consists of a

motorized rotation stage (ELL14K, Thorlabs) holding a half-wave plate positioned between two quarter-wave plates that are oriented orthogonally with respect to each other's fast axis. This arrangement effectively acts as a variable phase shifter for linearly polarized input light since:

$$\begin{aligned} J(\theta) &= \mathrm{QWP}\left(\tfrac{\pi}{4}\right)\cdot \mathrm{HWP}(\theta)\cdot \mathrm{QWP}\left(-\tfrac{\pi}{4}\right) \\ &= -\tfrac{i}{2}\begin{bmatrix} 1 & -i \\ -i & 1 \end{bmatrix}\begin{bmatrix} \cos^2\theta-\sin^2\theta & 2\sin\theta\cos\theta \\ 2\sin\theta\cos\theta & \sin^2\theta-\cos^2\theta \end{bmatrix}\begin{bmatrix} 1 & i \\ i & 1 \end{bmatrix} \\ &= \begin{bmatrix} 0 & e^{-i2\theta} \\ -e^{i2\theta} & 0 \end{bmatrix}. \end{aligned} \tag{19}$$

Here θ is the orientation of the fast axis of the half-wave plate. By rotating the half-wave plate at a fixed speed, the phase in one of the arms is varied continuously without changing the polarization, while the phase in the other arm remains constant on the timescale of the rotation. The two arms are then recombined at the fiber beam splitter, where the interference occurs and photons are directed towards two separate single-photon detectors. The matching of the timing and relative polarization of the two arms was ensured by interfering the excitation laser with itself and maximizing the contrast, which yielded a visibility of 98 %.

Extraction of the PNC from data

We follow ref. [14] to compute the PNC from the visibility. We remind that we only consider the *H*-polarized photons and stay in the approximation of the two-level system composed of the $|0\rangle$ and $|1\rangle$ Fock state. From the detector counts, we obtain the visibility v^{exp}, which is proportional to the occupation $\rho_{0,0}$. In the next step, we decompose the density matrix $\rho = \lambda\rho_{\mathrm{pure}} + (1-\lambda)\rho_{\mathrm{mixed}}$ into a part corresponding to a pure state and a part being a statistical mixture with the off-diagonal elements being zero. Note that we are only interested in the absolute value of the coherence and not in its phase. Following ref. [14], the visibility can be approximated by $v \approx \lambda^2\rho_{0,0}\sqrt{V_{\mathrm{HOM}}}$ with $0 \le \lambda \le 1$ and V_{HOM} being the photon indistinguishability. Considering the slope of the visibility as a function of $\rho_{0,0} = (1-\rho_{1,1})$ allows us to extract λ (see Supplementary Methods—Estimation of λ for PNC extraction from visibility). Together with the knowledge of $\rho_{1,1}$ via the photon counts, we can estimate the PNC as

$$\mathrm{PNC}^{\mathrm{exp.}} = \lambda\sqrt{\rho_{1,1}(1-\rho_{1,1})}\,. \tag{20}$$

DATA AVAILABILITY

The datasets generated and analyzed during the current study are available in the Zenodo repository, accessible via the following https://doi.org/10.5281/zenodo.7961599.

CODE AVAILABILITY

The code used for the simulation during the current study is available from the corresponding author on reasonable request.

Received: 4 August 2023; Accepted: 11 January 2024;
Published online: 27 January 2024

REFERENCES

1. Gisin, N. & Thew, R. Quantum communication. *Nat. Photon.* **1**, 165–171 (2007).
2. Briegel, H. J., Browne, D. E., Dür, W., Raussendorf, R. & Nest, M. Measurement-based quantum computation. *Nat. Phys.* **5**, 19–26 (2009).
3. Flamini, F., Spagnolo, N. & Sciarrino, F. Photonic quantum information processing: a review. *Rep. Prog. Phys.* **82**, 016001 (2018).
4. Pirandola, S. et al. Advances in quantum cryptography. *Advan. Opt. Photon.* **12**, 1012–1236 (2020).
5. Bennett, C.H. et al. Quantum cryptography: public key distribution and coin tossing. In: *Proceedings of IEEE International Conference on Computers, Systems, and Signal Processing* (IEEE, 1984).
6. Ekert, A. K. Quantum cryptography based on Bell's theorem. *Phys. Rev. Lett.* **67**, 661 (1991).
7. Briegel, H.-J., Dür, W., Cirac, J. I. & Zoller, P. Quantum repeaters: the role of imperfect local operations in quantum communication. *Phys. Rev. Lett.* **81**, 5932 (1998).
8. Lo, H.-K., Curty, M. & Qi, B. Measurement-device-independent quantum key distribution. *Phys. Rev. Lett.* **108**, 130503 (2012).
9. Vajner, D. A., Rickert, L., Gao, T., Kaymazlar, K. & Heindel, T. Quantum communication using semiconductor quantum dots. *Adv. Quantum Technol.* **5**, 2100116 (2022).
10. Hanschke, L. et al. Quantum dot single-photon sources with ultra-low multi-photon probability. *npj Quantum Inf.* **4**, 43 (2018).
11. Tomm, N. et al. A bright and fast source of coherent single photons. *Nat. Nanotechnol.* **16**, 399–403 (2021).
12. Zhai, L. et al. Quantum interference of identical photons from remote GaAs quantum dots. *Nat. Nanotechnol.* **17**, 829–833 (2022).
13. Uppu, R. et al. Scalable integrated single-photon source. *Sci. Adv.* **6**, 8268 (2020).
14. Loredo, J. et al. Generation of non-classical light in a photon-number superposition. *Nat. Photon.* **13**, 803–808 (2019).
15. Wein, S. C. et al. Photon-number entanglement generated by sequential excitation of a two-level atom. *Nature Photon.* **16**, 374–379 (2022).
16. Gottesman, D., Lo, H.-K., Lutkenhaus, N., & Preskill, J. Security of quantum key distribution with imperfect devices. In: IEEE (ed.) *International Symposium on Information Theory, 2004. ISIT 2004. Proceedings*, p. 136 https://doi.org/10.1109/ISIT.2004.1365172 (IEEE, 2004).
17. Lim, C. C. W., Curty, M., Walenta, N., Xu, F. & Zbinden, H. Concise security bounds for practical decoy-state quantum key distribution. *Phys. Rev. A* **89**, 022307 (2014).
18. Bozzio, M. et al. Enhancing quantum cryptography with quantum dot single-photon sources. *npj Quant. Inf.* **8**, 1–8 (2022).
19. Lo, H.-K. & Preskill, J. Phase randomization improves the security of quantum key distribution. https://arxiv.org/abs/quant-ph/0504209 (2005).
20. Tang, Y.-L. et al. Source attack of decoy-state quantum key distribution using phase information. *Phys. Rev. A* **88**, 022308 (2013).
21. Lo, H.-K. & Preskill, J. Security of quantum key distribution using weak coherent states with nonrandom phases. https://arxiv.org/abs/quant-ph/0610203 (2006).
22. Zhao, Y., Qi, B. & Lo, H.-K. Experimental quantum key distribution with active phase randomization. *Appl. Phys. Lett.* **90**, 044106 (2007).
23. Kobayashi, T., Tomita, A. & Okamoto, A. Evaluation of the phase randomness of a light source in quantum-key-distribution systems with an attenuated laser. *Phys. Rev. A* **90**, 032320 (2014).
24. Wang, X.-B. Beating the photon-number-splitting attack in practical quantum cryptography. *Phys. Rev. Lett.* **94**, 230503 (2005).
25. Bruß, D. Optimal eavesdropping in quantum cryptography with six states. *Phys. Rev. Lett.* **81**, 3018 (1998).
26. Scarani, V., Acin, A., Ribordy, G. & Gisin, N. Quantum cryptography protocols robust against photon number splitting attacks for weak laser pulse implementations. *Phys. Rev. Lett.* **92**, 057901 (2004).
27. Lucamarini, M. & Mancini, S. Secure deterministic communication without entanglement. *Phys. Rev. Lett.* **94**, 140501 (2005).
28. Berlin, G. et al. Experimental loss-tolerant quantum coin flipping. *Nat. Commun.* **2**, 561 (2011).
29. Pappa, A. et al. Experimental plug and play quantum coin flipping. *Nat. Commun.* **5**, 3717 (2014).
30. Pastawski, F., Yao, N. Y., Jiang, L., Lukin, M. D. & Cirac, J. I. Unforgeable noise-tolerant quantum tokens. *Proc. Natl Acad. Sci. USA* **109**, 16079–16082 (2012).
31. Bozzio, M. et al. Experimental investigation of practical unforgeable quantum money. *npj Quant. Inf.* **4**, 5 (2018).
32. Ng, N. H. Y., Joshi, S. K., Chen Ming, C., Kurtsiefer, C. & Wehner, S. Experimental implementation of bit commitment in the noisy-storage model. *Nat. Commun.* **3**, 1326 (2012).
33. Santos, M. B., Mateus, P. & Pinto, A. N. Quantum oblivious transfer: a short review. *Entropy* **24**, 945 (2022).
34. Lucamarini, M., Yuan, Z. L., Dynes, J. F. & Shields, A. J. Overcoming the rate–distance limit of quantum key distribution without quantum repeaters. *Nature* **557**, 400–403 (2018).
35. Lüker, S. & Reiter, D. E. A review on optical excitation of semiconductor quantum dots under the influence of phonons. *Semicond. Sci. Technol.* **34**, 63002 (2019).
36. Stufler, S. et al. Two-photon Rabi oscillations in a single $In_xGa_{1-x}As/GaAs$ quantum dot. *Phys. Rev. B* **73**, 125304 (2006).

37. Jayakumar, H. et al. Deterministic photon pairs and coherent optical control of a single quantum dot. *Phys. Rev. Lett.* **110**, 135505 (2013).
38. Barth, A. M. et al. Fast and selective phonon-assisted state preparation of a quantum dot by adiabatic undressing. *Phys. Rev. B* **94**, 45306 (2016).
39. Reindl, M. et al. Highly indistinguishable single photons from incoherently excited quantum dots. *Phys. Rev. B* **100**, 155420 (2019).
40. Cosacchi, M., Ungar, F., Cygorek, M., Vagov, A. & Axt, V. M. Emission-frequency separated high quality single-photon sources enabled by phonons. *Phys. Rev. Lett.* **123**, 17403 (2019).
41. Thomas, S. E. et al. Bright polarized single-photon source based on a linear dipole. *Phys. Rev. Lett.* **126**, 233601 (2021).
42. Bracht, T. K. et al. Swing-UP of Quantum Emitter Population Using Detuned Pulses. *PRX Quant.* **2**, 40354 (2021).
43. Karli, Y. et al. Super scheme in action: experimental demonstration of red-detuned excitation of a quantum emitter. *Nano Lett.* **22**, 6567–6572 (2022).
44. Koong, Z. X. et al. Coherent dynamics in quantum emitters under dichromatic excitation. *Phys. Rev. Lett.* **126**, 47403 (2021).
45. Wilbur, G. et al. Notch-filtered adiabatic rapid passage for optically driven quantum light sources. *APL Photon.* **7**, 111302 (2022).
46. Schöll, E. et al. Crux of using the cascaded emission of a three-level quantum ladder system to generate indistinguishable photons. *Phys. Rev. Lett.* **125**, 233605 (2020).
47. Akimov, I., Andrews, J. & Henneberger, F. Stimulated emission from the biexciton in a single self-assembled ii-vi quantum dot. *Phys. Rev. Lett.* **96**, 067401 (2006).
48. Sbresny, F. et al. Stimulated generation of indistinguishable single photons from a quantum ladder system. *Phys. Rev. Lett.* **128**, 093603 (2022).
49. Yan, J. et al. Double-pulse generation of indistinguishable single photons with optically controlled polarization. *Nano Lett.* **22**, 1483–1490 (2022).
50. Wei, Y. et al. Tailoring solid-state single-photon sources with stimulated emissions. *Nat. Nanotechnol.* **17**, 470–476 (2022).
51. Reiter, D. E., Kuhn, T. & Axt, V. M. Distinctive characteristics of carrier-phonon interactions in optically driven semiconductor quantum dots. *Adv. Phys. X* **4**, 1655478 (2019).
52. Cosacchi, M. et al. Accuracy of the quantum regression theorem for photon emission from a quantum dot. *Phys. Rev. Lett.* **127**, 100402 (2021).
53. Barth, A. M., Vagov, A. & Axt, V. M. Path-integral description of combined Hamiltonian and non-Hamiltonian dynamics in quantum dissipative systems. *Phys. Rev. B* **94**, 125439 (2016).
54. Besombes, L., Kheng, K., Marsal, L. & Mariette, H. Acoustic phonon broadening mechanism in single quantum dot emission. *Phys. Rev. B* **63**, 155307 (2001).
55. Machnikowski, P. & Jacac, L. Resonant nature of phonon-induced damping of Rabi oscillations in quantum dots. *Phys. Rev. B* **69**, 193302 (2004).
56. Cygorek, M., Barth, A. M., Ungar, F., Vagov, A. & Axt, V. M. Nonlinear cavity feeding and unconventional photon statistics in solid-state cavity qed revealed by many-level real-time path-integral calculations. *Phys. Rev. B* **96**, 201201 (2017).
57. Huber, D. et al. Highly indistinguishable and strongly entangled photons from symmetric GaAs quantum dots. *Nat. Commun.* **8**, 15506 (2017).
58. Silva, S. F. C. et al. Gaas quantum dots grown by droplet etching epitaxy as quantum light sources. *Appl. Phys. Lett.* **119**, 120502 (2021).
59. Bennett, C. H., Brassard, G., Crépeau, C.,= & Skubiszewska, M.-H. Practical quantum oblivious transfer. In: Feigenbaum, J. (ed.) *Advances in Cryptology—CRYPTO'91: Proceedings.* 351–366 https://link.springer.com/chapter/10.1007/3-540-46766-1_29 (2001).
60. Pan, J.-W., Bouwmeester, D., Weinfurter, H. & Zeilinger, A. Experimental entanglement swapping: entangling photons that never interacted. *Phys. Rev. Lett.* **80**, 3891 (1998).
61. Bouwmeester, D. et al. Experimental quantum teleportation. *Nature* **390**, 575–579 (1997).
62. González-Ruiz, E. M., Das, S. K., Lodahl, P. & Sørensen, A. S. Violation of bell's inequality with quantum-dot single-photon sources. *Phys. Rev. A* **106**, 012222 (2022).

ACKNOWLEDGEMENTS

The authors gratefully acknowledge insightful discussions with Stefan Frick, Robert Keil, Tommaso Faleo, Mathieu Bozzio and Serkan Ates. Nils Kewitz and Bhavana Panchumarthi supported the early phases of the experiment. Y.K., F.K., R.S., V.R. and G.W. acknowledge financial support through the Austrian Science Fund FWF projects W1259 (DK-ALM Atoms, Light, and Molecules), FG 5, TAI-556N (DarkEneT), F 7114 (BeyondC) and I4380 (AEQuDot). DAV and TH acknowledge financial support by the German Federal Ministry of Education and Research (BMBF) via projects 13N14876 ('QuSecure') and 16KISQ087K (tubLAN Q.0). TKB and DER acknowledge financial support from the German Research Foundation DFG through project 428026575 (AEQuDot). A.R. and SFCdS acknowledge the FWF projects FG 5, P 30459, I 4320, the Linz Institute of Technology (LIT) and the European Union's Horizon 2020 research, and innovation program under Grant Agreement Nos. 899814 (Qurope), 871130 (ASCENT+) and the QauntERA II Program (project QD-E-QKD). L.M.H., P.W. and J.C.L. acknowledge financial support from the European Union's Horizon 2020 and Horizon Europe research and innovation program under grant agreement No 899368 (EPIQUS), the Marie Skłodowska-Curie grant agreement No 956071 (AppQInfo), and the QuantERA II Program under Grant Agreement No 101017733 (PhoMemtor); FWF through F7113 (BeyondC), and FG5 (Research Group 5); from the Austrian Federal Ministry for Digital and Economic Affairs, the National Foundation for Research, Technology and Development and the Christian Doppler Research Association. For the purpose of open access, the author has applied a CC BY public copyright licence to any Author Accepted Manuscript version arising from this submission.

AUTHOR CONTRIBUTIONS

The experimental setup was built by Y.K., F.K., R.S., V.R., J.C.L., D.A.V., L.M.H., and the measurements were performed by Y.K., F.K., D.A.V. The main numerical calculations were carried out by P.C.A.H., with supporting calculations provided by F.K and Y.K. The sample was provided by C.S., S.F.CdS, A.R. The first draft of the manuscript was written by D.A.V., F.K., Y.K., P.C.A.H., V.R., D.E.R. Conceptual work and supervision were done by G.W., P.W., V.M.A, D.E.R., V.R., J.C.L., T.H., A.R. All authors discussed the results and were involved in writing the manuscript.

COMPETING INTERESTS

The authors declare no competing interests.

ADDITIONAL INFORMATION

Supplementary information The online version contains supplementary material available at https://doi.org/10.1038/s41534-024-00811-2.

Correspondence and requests for materials should be addressed to Yusuf Karli.

Reprints and permission information is available at http://www.nature.com/reprints

Publisher's note Springer Nature remains neutral with regard to jurisdictional claims in published maps and institutional affiliations.